Supporting Information

Nanoplating SnO_2 thin-film on MXene-based sponge for stable and efficient solar energy conversion

Qi Zhang[1], Ze Fu[2], Hongtao Yu[1], Shuo Chen[1]*

[1]Key Laboratory of Industrial Ecology and Environmental Engineering (Ministry of Education, China), School of Environmental Science and Technology, Dalian University of Technology, Dalian 116024, China.

[2]School of Fisheries and Life Science, Dalian Ocean University, Dalian 116023, China.

E-mail: shuochen@dlut.edu.cn

Qi Zhang and Ze Fu contributed equally to this work.

1. Experimental

1.1 Synthesis of Ti_3C_2.

Ti_3C_2 (MXene) nanosheets solution was prepared by the following fabricating manufacturing procedures: Firstly, 0.5 g LiF powder was slowly added into a pre-configured 10 mL 9M HCl solution. Secondly, 0.5 g of the MAX phase precursor (Ti_3AlC_2) powder was added to the above mixed solution in multiple portions, and then the Al layer was etched at 35 °C with magnetic stirring for 24 h. Thirdly, the product was washed with water and centrifuged for several times until the pH> 6. Fourthly, the above product was sonicated under ice bath and an Ar atmosphere conditions for 1 h. Finally, after centrifugation for another 1 h at 3500 rpm, the dark green supernatant of MXene nanosheet was collected. The concentration of Ti_3C_2 nanosheet dispersion was determined through filtering a certain volume of the suspension and measuring the weight of the film after vacuum drying.

1.2 Synthesis of SPM.

The 3D porous MXene-based sponge (SPM) was prepared by a facile coating and calcination method. Typically, the MXene-coated sponge was fabricated by coating MXene nanosheets onto the skeleton of a sponge by a simple solution dipping-drying method. Typically, the commercial sponge (Wood pulp sponge, Germany) was carefully dipped into Ti_3C_2 solution (2 mg•mL^{-1}) for 24 h. The effect of the loading concentration of Ti_3C_2 (0.5, 1.0, 1.5, 2.0 and 2.5 mg•mL^{-1}) on the evaporation performance was investigated systematically, as shown in Fig. S20 and S21. MXene-coated sponge was freeze-dried overnight. Subsequently, the MXene-coated sponge was transferred in a ceramic boat and placed into a temperature-programmed furnace under Ar flow, heated from room temperature to 800 °C in 3 h, and then kept at 800 °C for 2 h and cooled down to room temperature, named as SPM_{800}. The SPMs under the different calcination temperatures (300, 500, 800 and 1000 °C) were fabricated, named as SPM_{300}, SPM_{500}, SPM_{800} and SPM_{1000}, respectively.

1.3 Synthesis of SnO_2-SPM.

6.78g of $SnCl_2$•$2H_2O$ was dissolved in 50 mL of ethanol solution, backflow and stir for 4 h in a three-necked flask at 80 °C. Subsequently, the heating is stopped, and the solution was sealed and placed at room temperature for 24 h to obtain a uniform and transparent pale yellow SnO_2 sol. The SnO_2-SPM was obtained by coating SnO_2 sol on the SPM using a dip-coating process. A dip coater (SYDC-100, Shanghai SAN-YAN Technology Co., Ltd, China) was used for coating SnO_2 sol on the SPM. The dipping time was set to 30 min and the lifting speed was 1 mm•s^{-1}. Here, the impregnation of SPM with SnO_2 sol was repeated 1, 3 or 5 times. The final products were calcined at 500 °C for 2 h with a heating/cooling rate of 2 °C•min^{-1}, named as SnO_2-SPM. The SnO_2 layer thickness of SnO_2-SPMs repeated 1, 3 and 5 impregnation times was 2.1, 5.6 and 11.2 nm, respectively, evaluated by the TEM images, named as SnO_2-$SPM_{2.1}$, SnO_2-$SPM_{5.6}$ and SnO_2-$SPM_{11.2}$, respectively.

1.4 Characterization.

Transmission electron microscopy (TEM, JEM-2100F) and scanning electron microscopy (SEM, Quanta 200 FEG) was used to analyze the morphology of the samples. The crystallinity of the samples was determined by X-ray diffractometer (XRD, EMPYREAN, PANalytical) using a diffractometer with Cu Kα radiation. Fourier transform infrared spectrum (FTIR) of the sample was obtained on KBr pellets on a spectrometer (Nicolet, Madison). X-ray photoelectron spectroscopy (XPS, VG ESCALAB250) was carried to analyze the elementary composition of samples. The optical transmittance and reflectance spectra of the surfaces of samples were recorded in the range of 200–2500 nm with a ultraviolet–visible–near-infrared spectrophotometer (UV-vis NIR spectra) equipped with an integrating sphere. The absorption efficiency was then calculated by $A = 1 - R - T$, where R and T are the reflection and transmission efficiency, respectively. FLUKE Ti 45 infrared camera was used to take infrared photographs. The mechanical strength of the samples was measured using a universal testing machine (AGS-X, Shimadzu Ltd., Japan). Water contact

angle of samples was tested on an optical contact angle & interface tension meter (SL200KB, Kino, USA).

1.5 Experimental Setup for Steam Generation.

The steam generation experiments were performed under a homemade optical system, with a solar simulator (KGS-40S3-TT, AM1.5). In the experiment, the water was contained by a chamber and the SnO_2-SPMs floated on the surface of the water. The mass change was measured by a balance (BSA3202S Max 3200g d=0.01g, Sartorius) for the evaluation of the evaporation rate and solar-thermal conversion efficiency. The four actual seawaters around China (Yellow sea, Bohai sea, East China sea and South China sea) and four salt waters from lakes in Tibet of China were taken for steam generation tests. During cycling test, after each cycle, the crystalline salt would be washed out and then the absorber would be dried in the air to simulate the actual use.

1.6 Water transport measurements.

The completely dried samples of SnO_2-SPM were immersed in DI water at room temperature. The weight of these samples was carefully tracked during the swollen process until they were fully hydrated. The record data from dried state to fully-hydrated was used to evaluate the water transport in SnO_2-SPMs.

1.7 Water evaporation performance under one-sun irradiation.

The water evaporation rate was calculated by the following equation:

$$v = \frac{d\dot{m}}{s \times dt}$$

where $\dot{m}$ is the mass flux, s is the illuminated area, t is time, and v is evaporation rate.

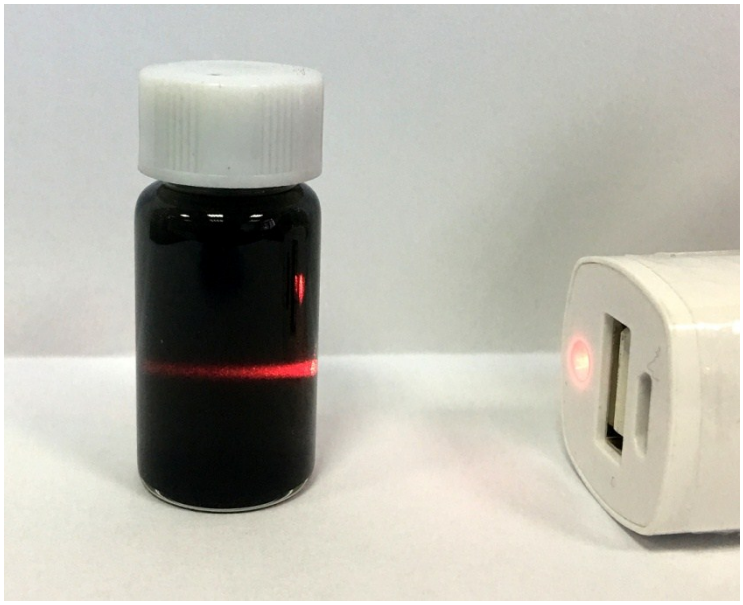

Fig. S1 The Tyndall effect of MXene solution.

The stable MXene nanosheet solution was prepared by etching the Ti_3AlC_2 precursor (MAX phase) with a mixture solution of LiF and HCl. The finally prepared Ti_3C_2 nanosheets aqueous solution showed good dispensability, which is proved by the apparent Tyndall scattering effect of the red laser passing through the solution (Fig. S1).

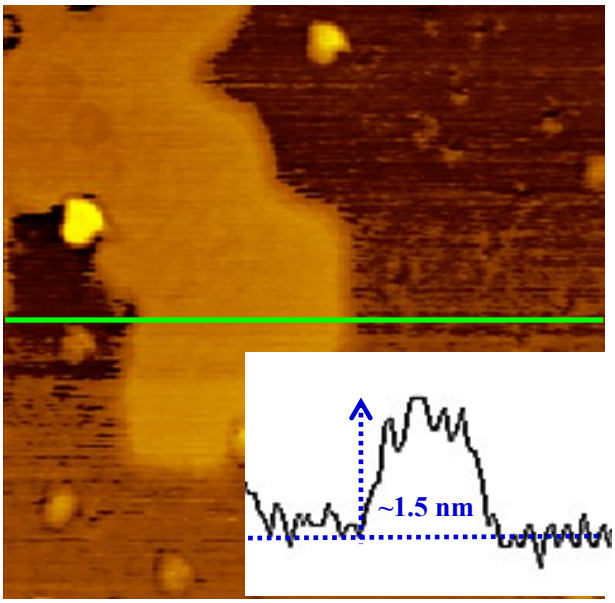

Fig. S2 AFM image and its height profile of MXene nanosheets.

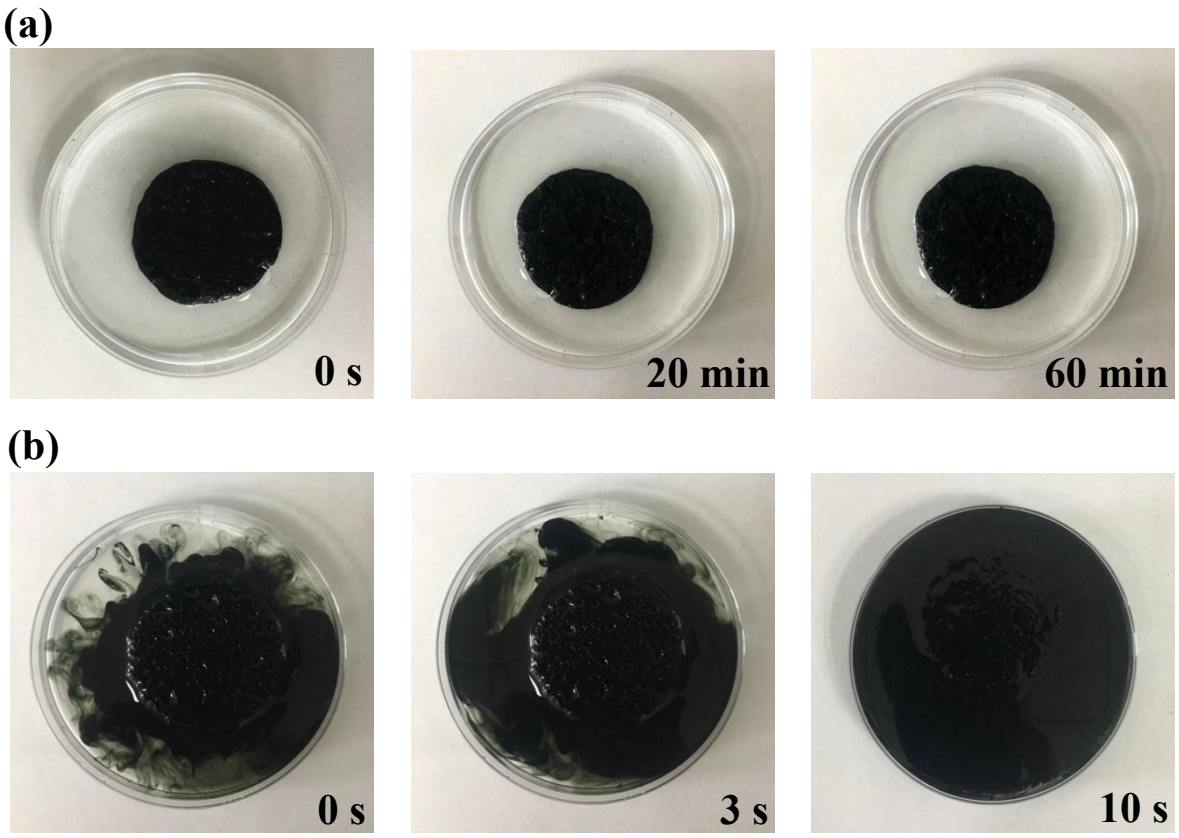

Fig. S3 Digital photographs of (a) the calcined MXene-coated sponge and (b) MXene-coated sponge without calcination soaked in water for some time.

Fig. S4 Photograph of SnO_2-SPM on a fragile *setaria viridis*, showing the ultralight performance of the synthesized SnO_2-SPM.

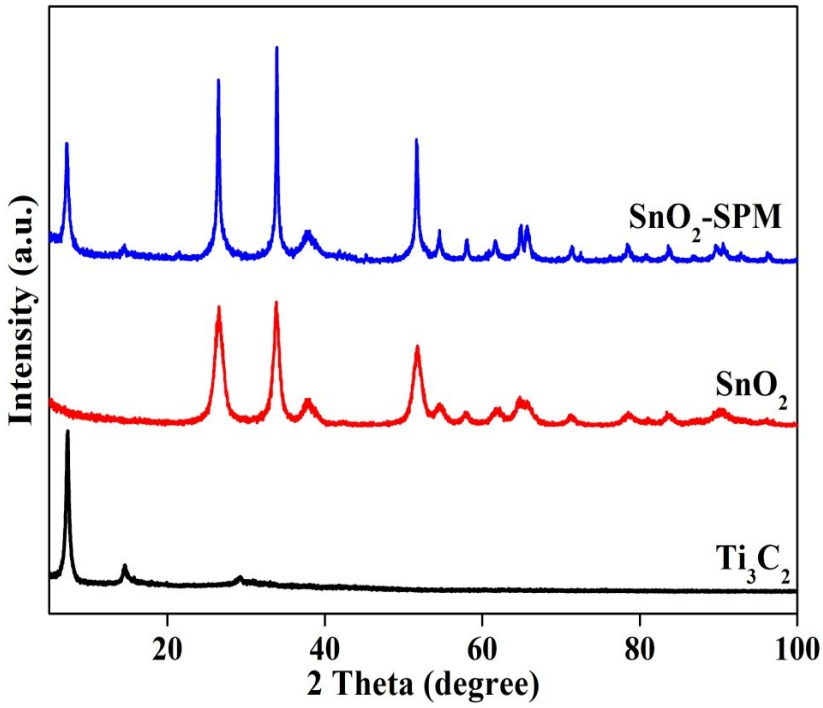

Fig. S5 XRD patterns of Ti_3C_2, SnO_2 and SnO_2-SPM.

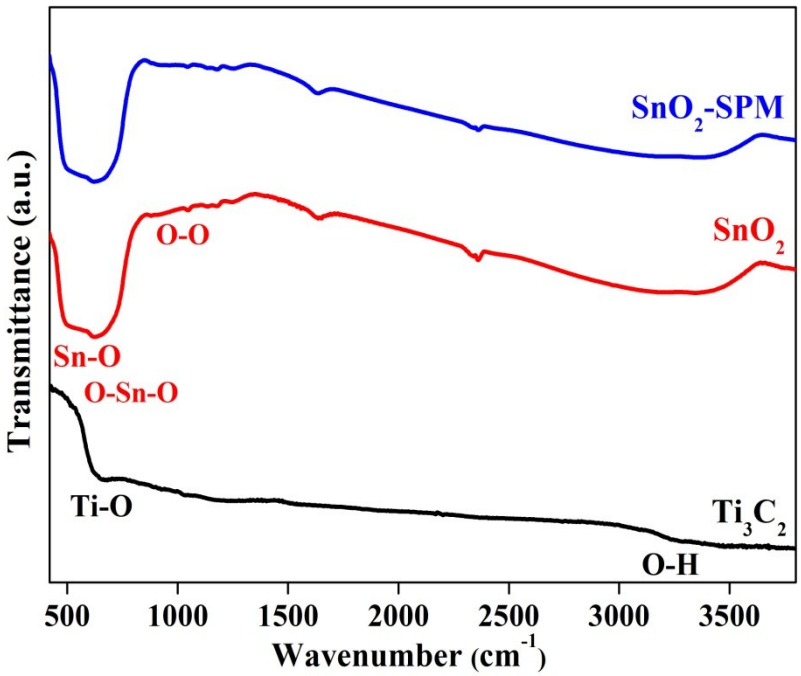

Fig. S6 FT-IR spectra of Ti_3C_2, SnO_2 and SnO_2-SPM.

Solar absorbers should have the efficient light absorption, which promotes light-water-steam production. Therefore, the thickness of SnO_2 layer nanoplating SPMs played an important role in the photothermal conversion of SnO_2-SPMs, because too thick SnO_2 layer was adverse to the light absorption and the heat transport from Ti_3C_2 to the top surface of SnO_2-SPM. The thickness of SnO_2 layer on SPM can be regulated by changed the coating times (see Method 1.3). As shown in Fig. S7, when the impregnation of SPM with SnO_2 sol was repeated 1, 3 or 5 times, the SnO_2 layer thickness was ~2.1, ~5.6 and ~11.2 nm for the SnO_2-$SPM_{2.1}$, SnO_2-$SPM_{5.6}$ and SnO_2-$SPM_{11.2}$, respectively. The absorption of SnO_2-SPMs with different SnO_2 layer thickness was carefully measured with an UV-vis NIR spectra equipped with an integrating sphere. As displayed in Fig. S8, the averaged absorption (weighted by AM1.5G solar spectrum) across 200–2500 nm is ~95% for SnO_2-$SPM_{2.1}$, which laid foundations for efficient solar vapour production. However, the absorption gradually decreased from ~95% (SnO_2-$SPM_{2.1}$) to ~88% (SnO_2-$SPM_{11.2}$) with the thickness increasing of SnO_2 layer. Besides, Figure S9 indicated that the surface temperature of SnO_2-SPMs decreased from 44.8 to 33.5 °C once the thickness of SnO_2 layer was increased from 2.1 to 11.2 nm after irradiation time of 600 s.

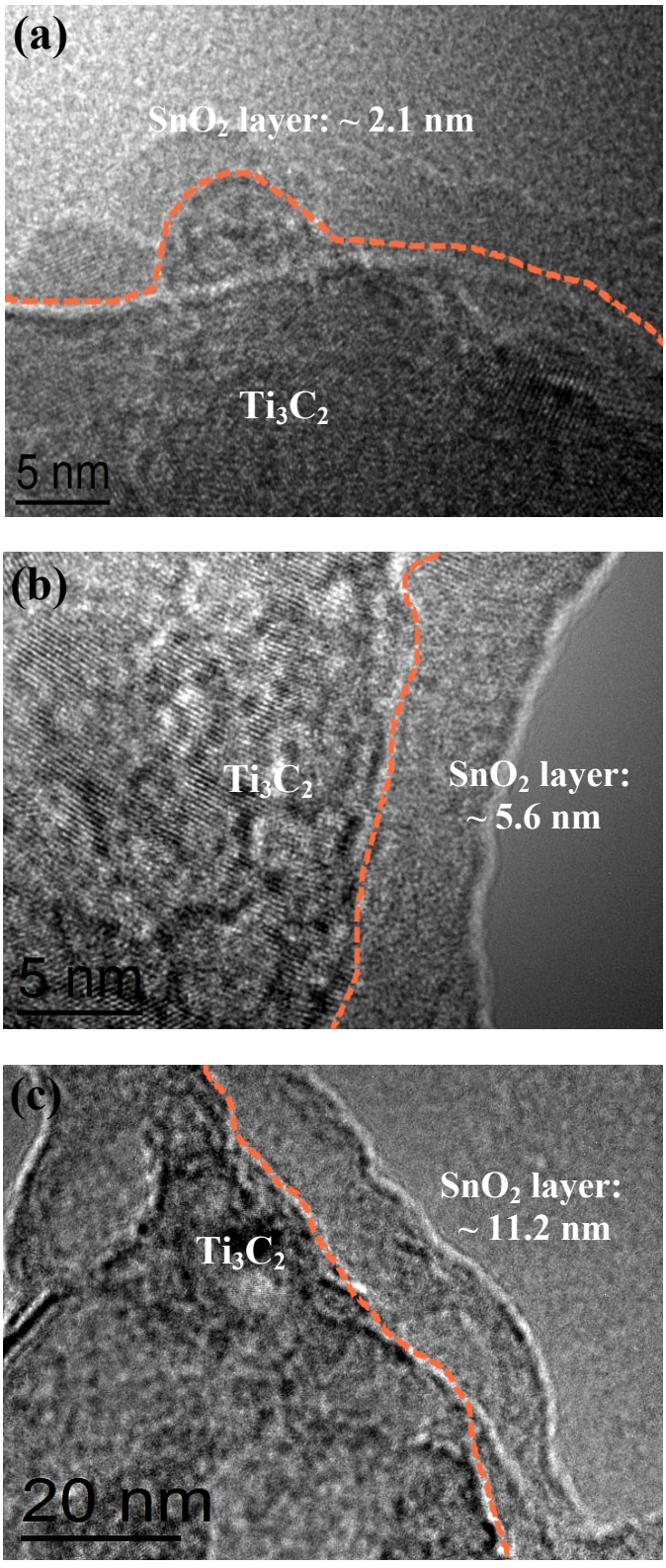

Fig. S7 TEM images of SnO_2-SPM samples with different SnO_2 layer thicknesses.

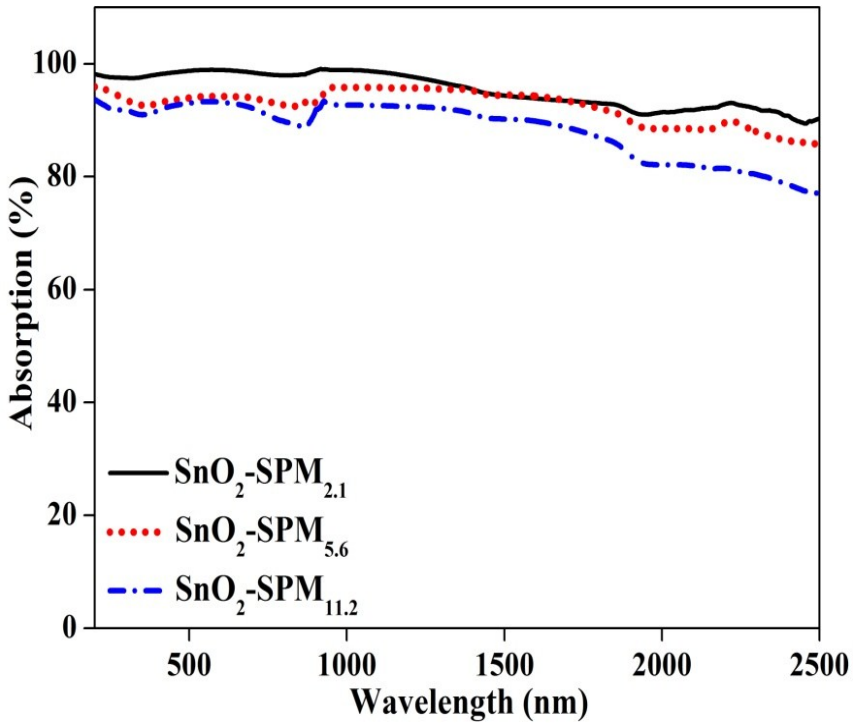

Fig. S8 UV-vis NIR spectra of SnO_2-SPM absorbers with different SnO_2 layer thickness.

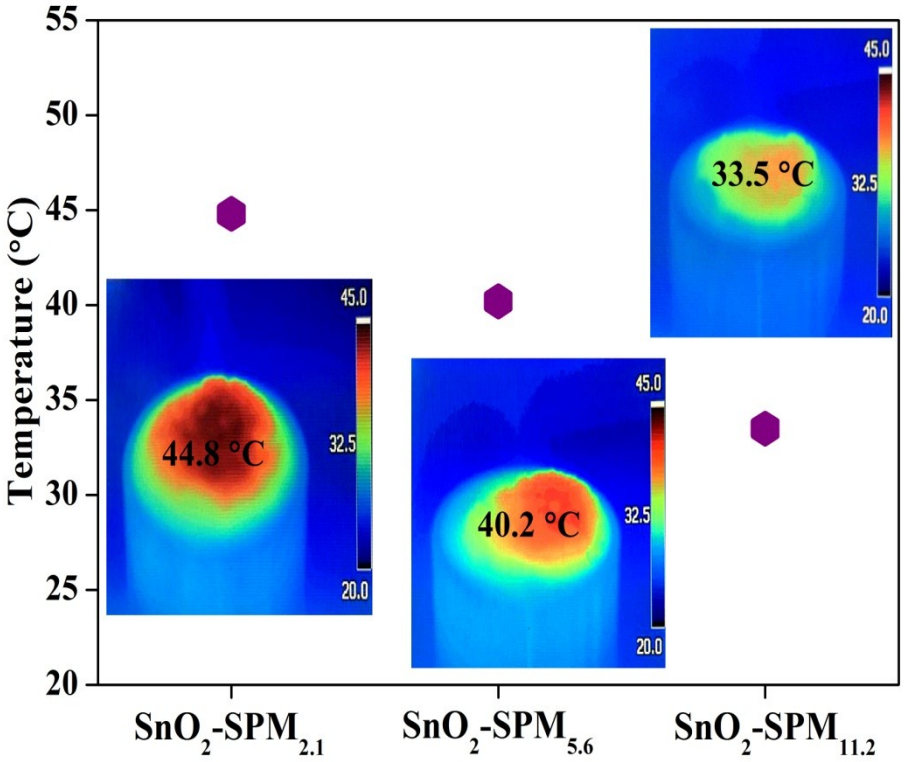

Fig. S9 The surface temperature of SnO_2-SPM samples at 600 s; Inset: infrared images showing the temperature distribution of SnO_2-SPM samples after irradiation time of 600 s.

Optimization of SnO_2-SPM calcination temperature.

Water transport in internal gaps and micron channels was highly dependent on the capillary pumping, while the porous structure and hydrophilicity had become particularly important for capillarity. Apart from offering water transporting channels, the porous network structure was also beneficial to reducing the thermal conductivity. The low thermal conductivity was favorable to heating the localized water, which was significant for efficient solar vapour production. Herein, the nanostructure was tuned by controlling calcination temperature and thus regulating the water content and transport in the SnO_2-SPMs with the optimized calcination temperature of 800 °C (Fig. S10–12). SnO_2-SPMs with calcination temperature of 300, 500, 800 and 1000 °C were prepared (designated as SnO_2-SPM_{300}, SnO_2-SPM_{500}, SnO_2-SPM_{800} and SnO_2-SPM_{1000}, respectively) to investigate the water transport of structure-dependence. The water evaporation rate of SnO_2-SPMs gradually increased and the hierarchical pore structure in SnO_2-SPMs was increasingly obvious with the increasing of calcination temperature from 300 to 1000 °C (Fig. S10 and S11). Additionally, the size of their micron channels also varied with the calcination temperature (Fig. S11), which resulted in the different mechanical properties. Experimental results in Fig. S12 showed that the mechanical strength of the SnO_2-SPMs decreased gradually with the calcination temperature from 300 to 1000 °C. The mechanical property further evidenced such difference among SnO_2-SPMs when the calcination temperature was changed.

The optimized calcination temperature of SnO_2-SPM is 800 °C in this work. An optimized calcination temperature can enable the accelerated solar vapor generation and reduce the cost of SnO_2-SPMs. As shown below, solar vapor generation of the control samples with SnO_2-SPM calcination temperature of 300, 500, 800 and 1000 °C, designating as SnO_2-SPM_{300}, SnO_2-SPM_{500}, SnO_2-SPM_{800} and SnO_2-SPM_{1000}, respectively, were tested under one sun. Fig. S10 shows that SnO_2-SPM_{800} has a higher evaporation rate compared with

SnO_2-SPM_{300} and SnO_2-SPM_{500}. In addition, it could be found the evaporation rate of SnO_2-SPM_{1000} was only slightly higher than that of SnO_2-SPM_{800}.

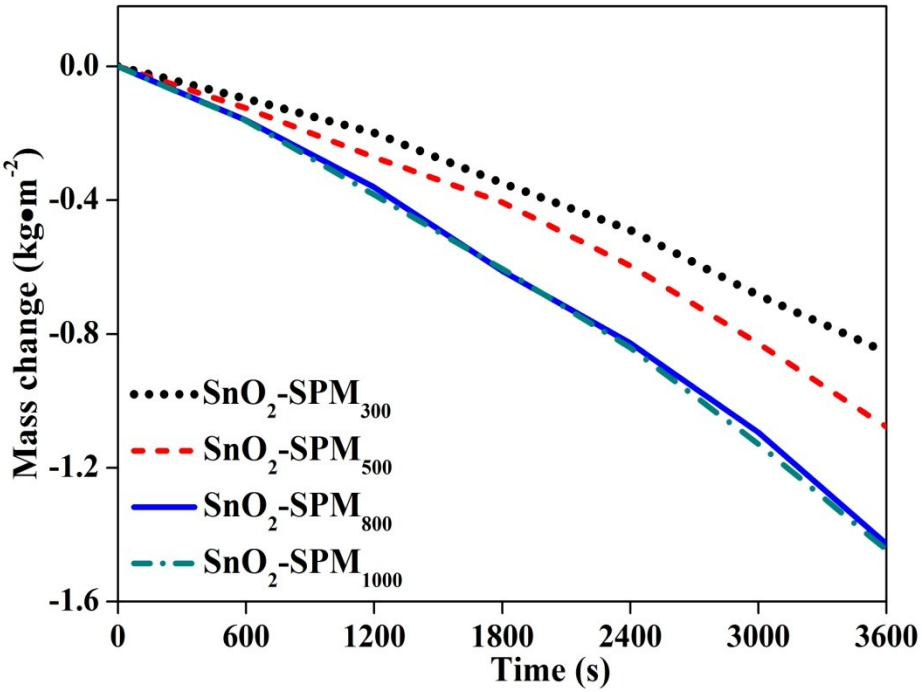

Fig. S10 Mass change over time with SnO_2-SPM_{300}, SnO_2-SPM_{500}, SnO_2-SPM_{800} and SnO_2-SPM_{1000}.

As shown in Fig. S11, the size of micro-channels of SnO_2-SPMs gradually enlarged with the increase of calcination temperature. The SnO_2-SPM_{800} and SnO_2-SPM_{1000} exhibited the large micro-channels, while the SnO_2-SPM_{300} and SnO_2-SPM_{500} only provide the small micro-channels. In addition, it can be also found that the internal gaps of SnO_2-SPM disappeared when the calcination temperature was up to 1000 °C. Thus, the calcination temperature of SnO_2-SPMs should be at 800 °C to achieve the hierarchical nanostructure. This hierarchical nanostructure was beneficial to the water vapor transport.

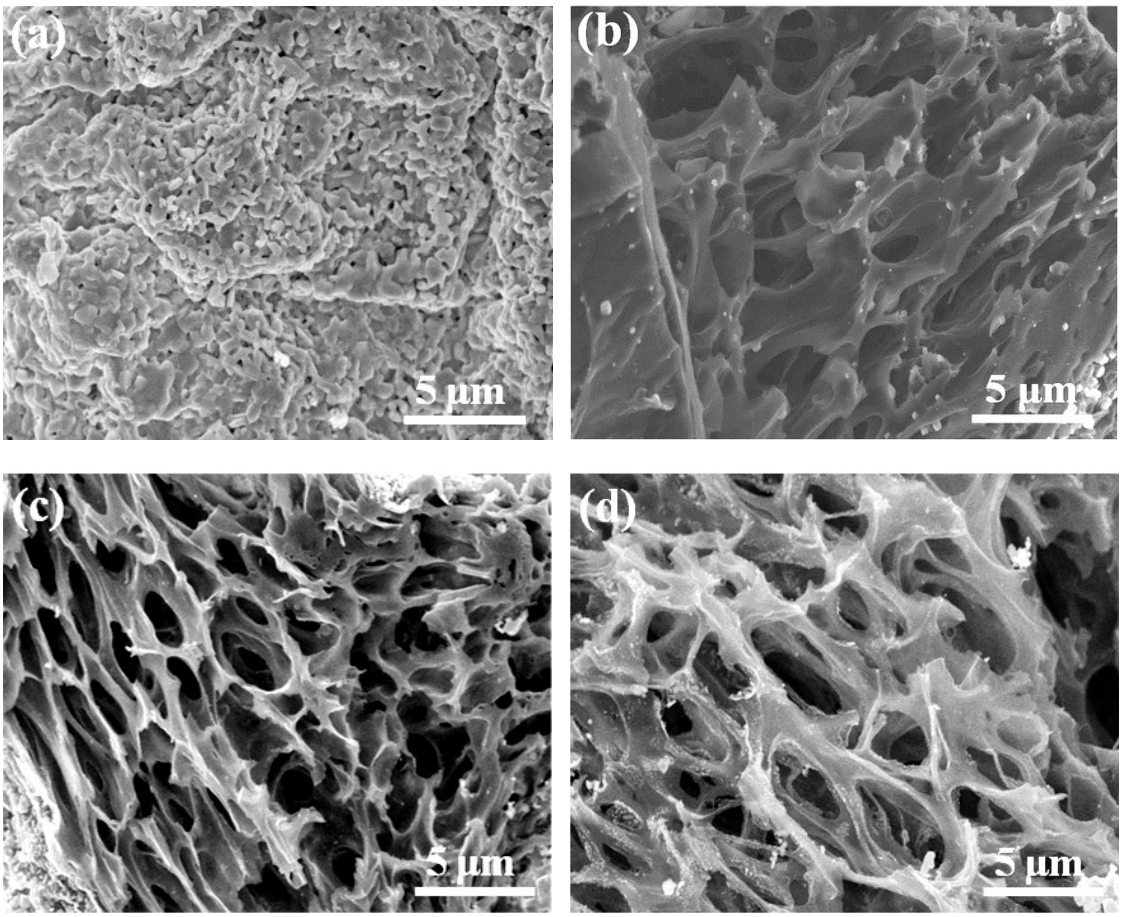

Fig. S11 SEM images of (a) SnO_2-SPM_{300}, (b) SnO_2-SPM_{500}, (c) SnO_2-SPM_{800} and (d) SnO_2-SPM_{1000}, showing the micron channel structure with different size.

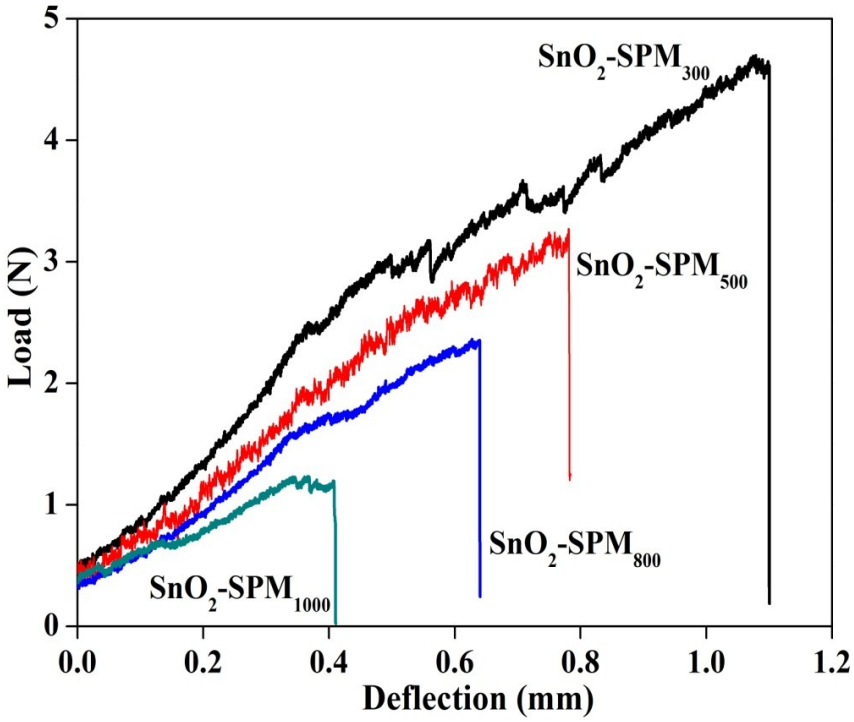

Fig. S12 Mechanical properties of SnO_2-SPMs.

The water content (Q) was calculated with the water mass in the fully swollen absorber divided of corresponding dried mass of absorber. The saturated water content (Qs) of SnO_2-SPM_{800} was ~10 g•g^{-1}, which was ~1.6 and ~3.4 times those of the SnO_2-SPM_{500} and SnO_2-SPM_{300}, respectively, suggesting that a wide range of Qs could be obtained *via* changing the calcination temperature (Fig. S13a). Here it could be found the Qs value of SnO_2-SPM_{1000} was only slightly higher than that of SnO_2-SPM_{800}. The water transport in SnO_2-SPMs was evaluated by the analysis of the water-uptake dynamic process. The water-uptake time from fully dried state to saturated state revealed the water transport in the SnO_2-SPMs (Fig. S13b). Since the Q values of all SnO_2-SPM samples showed a linear dependence on time during the water-uptake, a water transport rate (V) was defined as water absorption per minute. The SnO_2-SPM_{300}, SnO_2-SPM_{500}, SnO_2-SPM_{800} and SnO_2-SPM_{1000} showed V value of 0.016, 0.73, 0.17 and 0.18 g•min^{-1}, respectively (Fig. S13b), indicating that the V value was affected by the nanostructured channels.

Hydrophilicity was vital for pumping seawater to the hot surface of absorbers by capillarity, thus, the water contact angle was determined to investigate the wetting property of SnO_2-SPMs. Due to the fast permeating of water into SnO_2-SPMs, the water permeating time, defined as the water droplet from just contacting the SnO_2-SPM surface to fully permeate into the SnO_2-SPM interior, was used to represent the hydrophilicity of SnO_2-SPMs with different calcination temperature. With the increase of calcination temperature, the water permeating time of SnO_2-SPM absorbers gradually decreased from 801 to 327 ms, as shown in Fig. S13c. Hence, water can quickly permeate and pass through the interconnected pores of SnO_2-SPM absorbers, thereby insuring the sufficient supply of water during vapour generation.

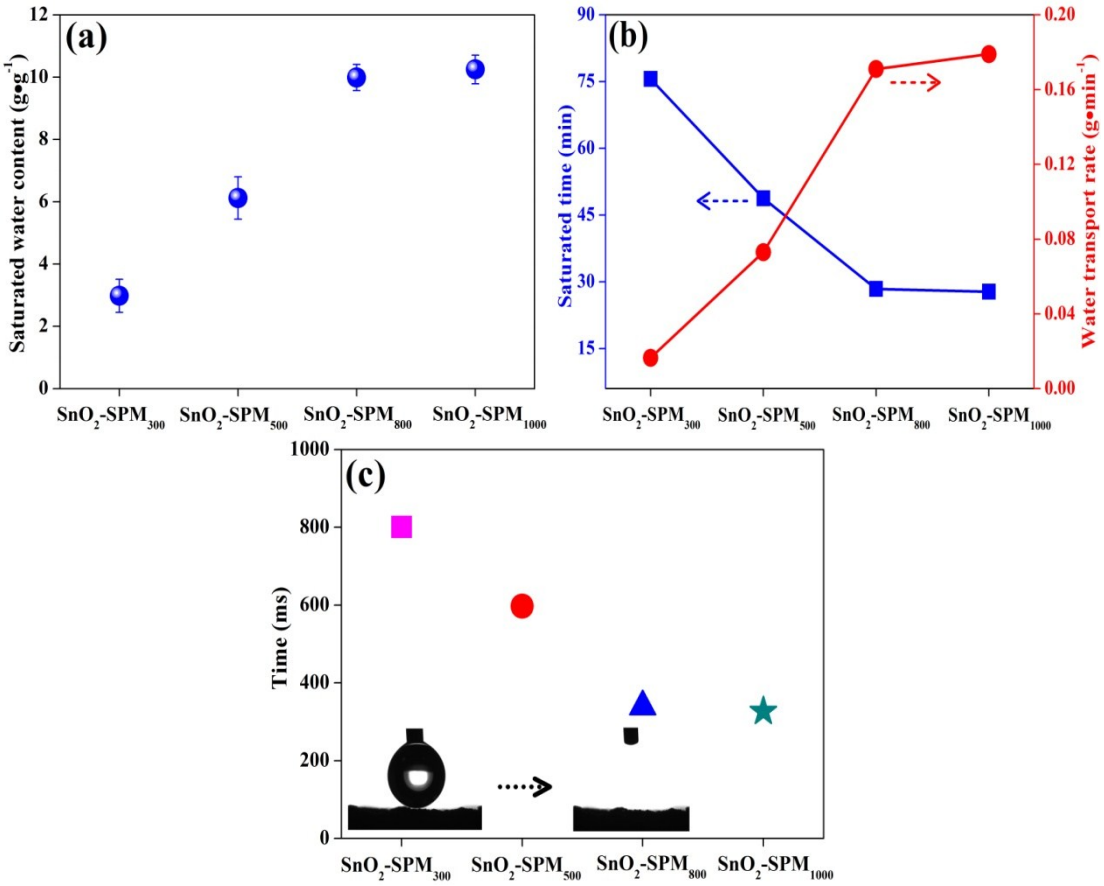

Fig. S13 (a) Saturated water content in SnO_2-SPMs per gram of corresponding dried samples; (b) Swollen behaviour from the fully dried state to the saturated state and the calculated water transport rate showing the tunable water transport ability of the SnO_2-SPM_{300}, SnO_2-SPM_{500}, SnO_2-SPM_{800} and SnO_2-SPM_{1000} represent absorbers with calcination temperature of 300, 500, 800 and 1000 °C, respectively; (c) Time variations of water droplet from just contacting SnO_2-SPM surface to fully permeate into SnO_2-SPM interior.

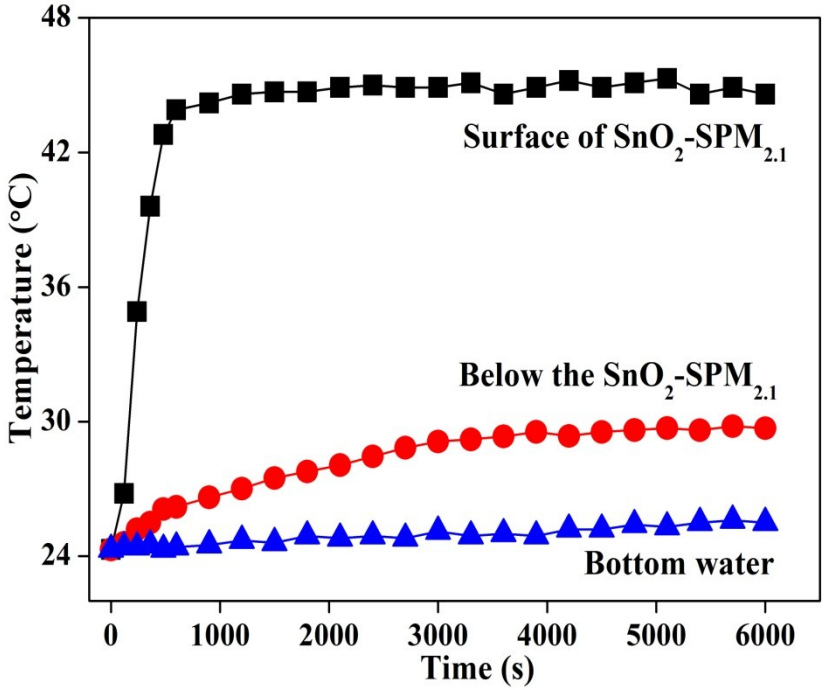

Fig. 14 The temperature rise of bottom water, below surface the SnO_2-$SPM_{2.1}$, and top surface of SnO_2-$SPM_{2.1}$ in the cuvette.

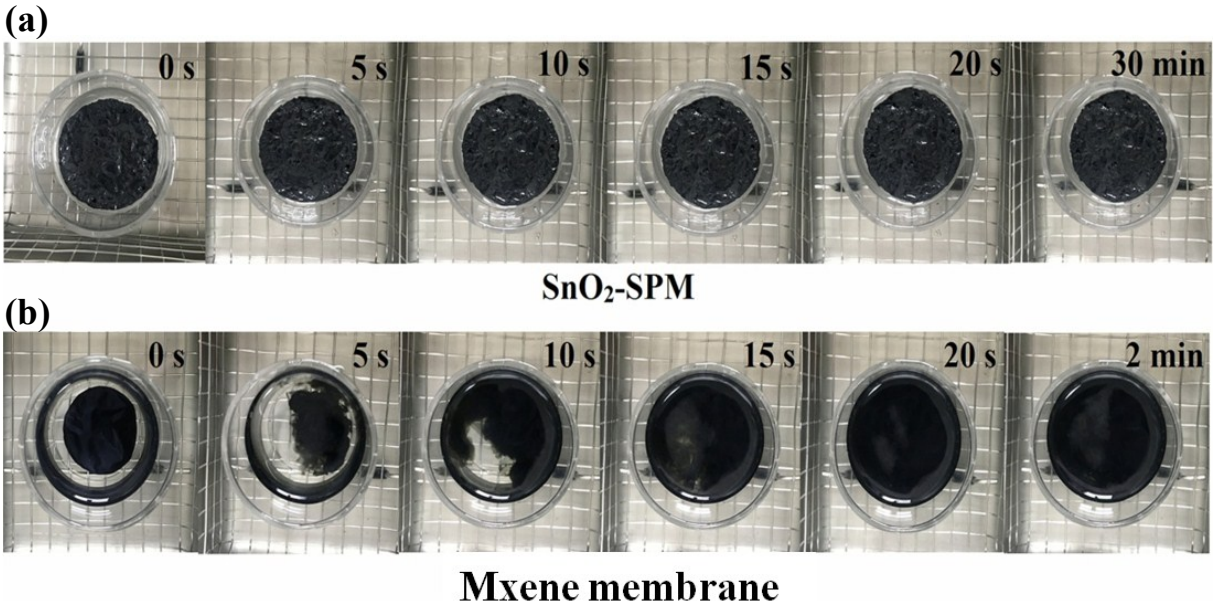

Fig. S15 Video snapshots of (a) the SnO_2-SPM and (b) the MXene membrane, which was prepared according to the methods reported [1] being soaked in water under bath sonication for different periods. The water tolerant of MXene membrane has a poor long-term stability in water. Fortunately, our lightweight SnO_2-SPM floating on the water retained the perfect structural integrity after the bath sonication for 30 min, whereas the MXene membrane sank to the bottom of the container and started to decompose when it was sonicated for 5 s under the same conditions, and it completely disintegrated within 20 s.

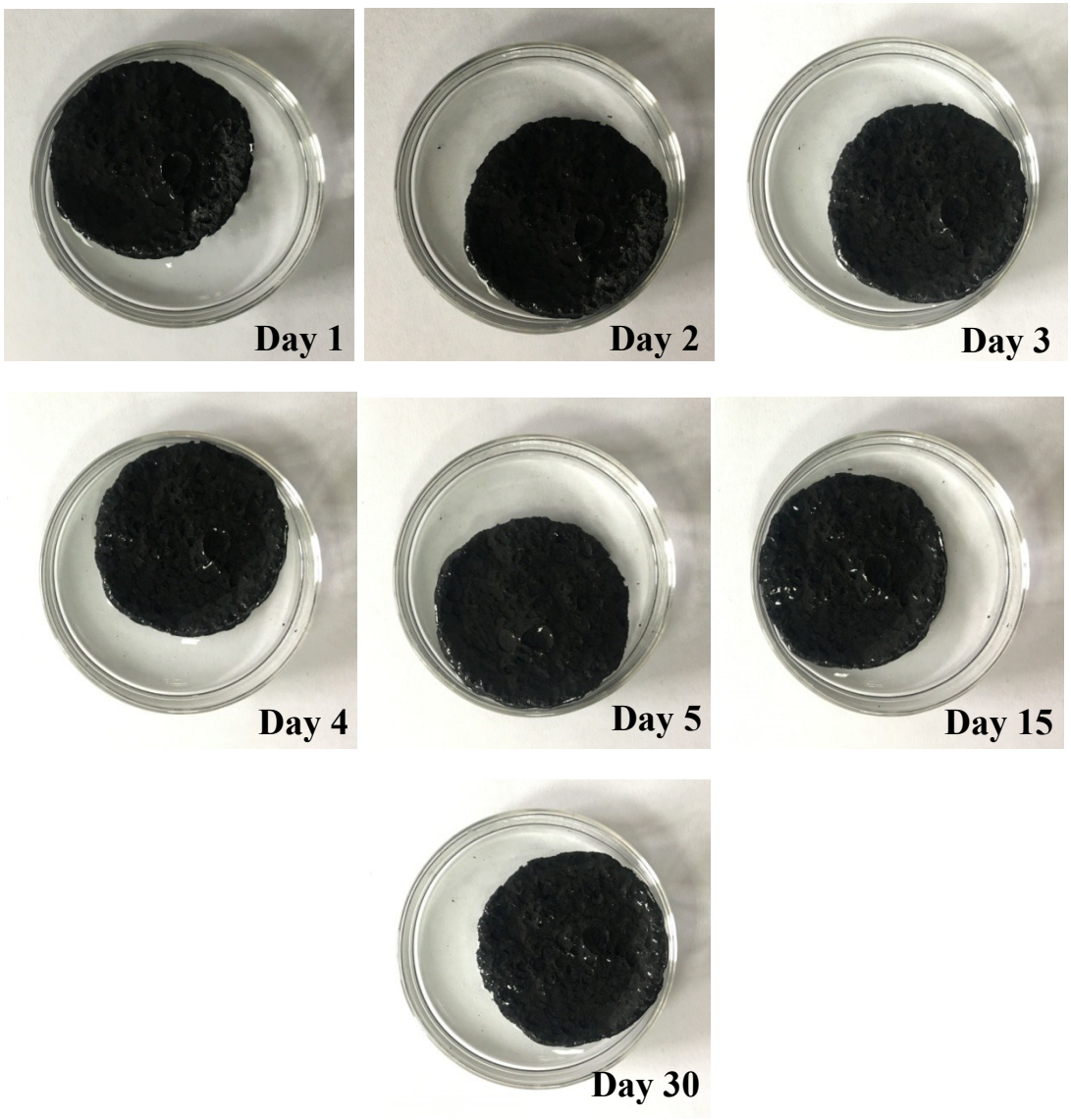

Fig. S16 Digital photos showing the long-term stability by soaking the SnO_2-SPM into water for 30 d.

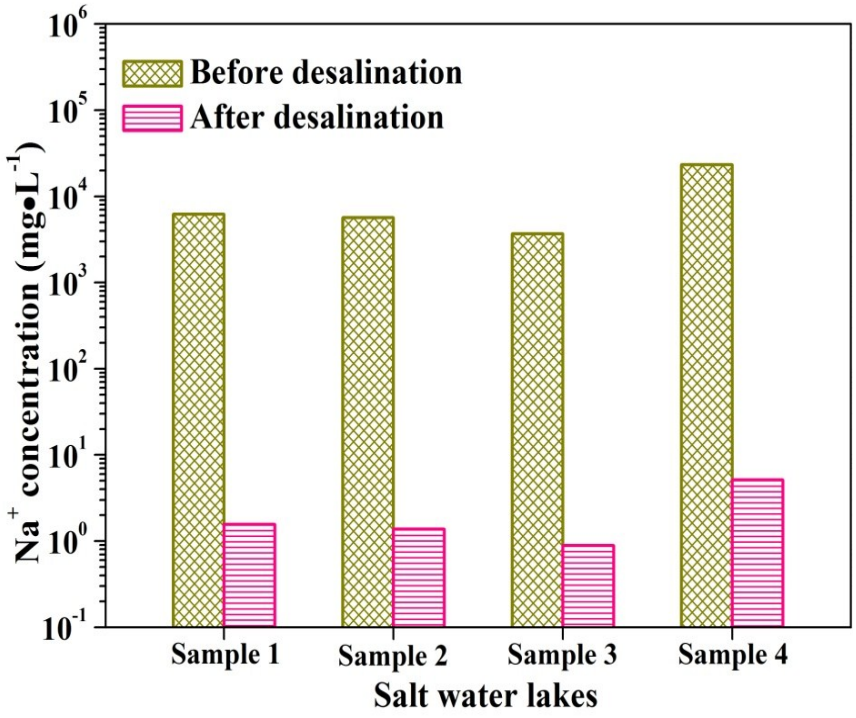

Fig. S17 Na^+ concentrations of four actual salt water lakes (Tibet, China) before and after desalination.

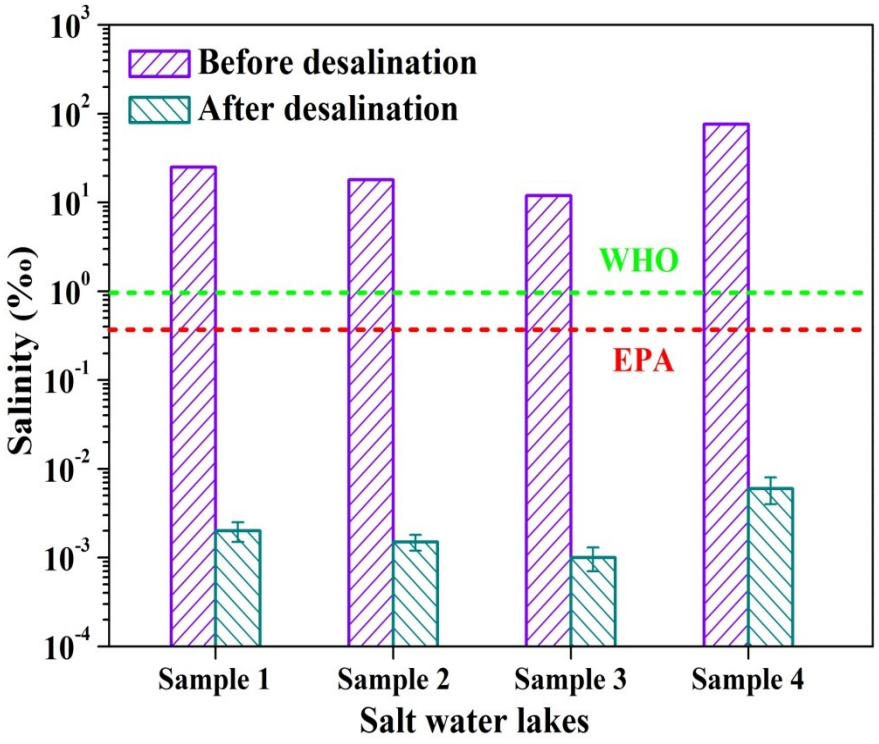

Fig. S18 The salinities of four brackish water samples before and after desalination using SnO_2-$SPM_{2.1}$. The broken lines refer to the World Health Organization (WHO, green line) and US Environmental Protection Agency (EPA, red line) salinity standards for drinkable water.

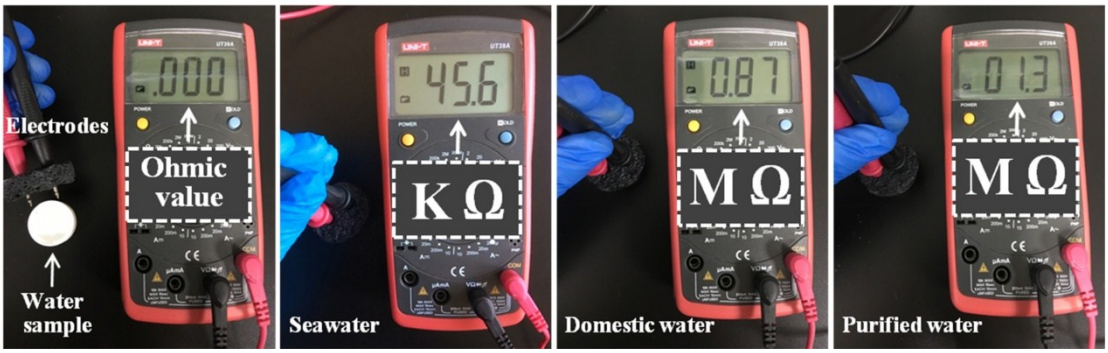

Fig. S19 Evaluation of water purity using a multimeter with a constant distance between electrodes. The results demonstrated a high purity of purified water, similar to that of domestic water.

Table S1. Water quality parameters of four actual seawaters and salt water lakes.

	Yellow sea	**Bohai sea**	**East China sea**	**South China sea**	**Salt water lake 1**	**Salt water lake 2**	**Salt water lake 3**	**Salt water lake 4**
pH	7.9	7.9	7.8	7.8	9.4	9.7	9.6	9.3
Salinity (‰)	31.0	30.0	32.0	35.0	25.0	18.0	12.0	76.0
Basicity ($mmol•L^{-1}$)	20.4	21.7	18.7	22.1	37.2	106.2	36.3	87.7
HCO_3^- ($mmol•L^{-1}$)	15.4	18.4	16.7	17.9	6.5	34.3	12.1	12.5
$1/2CO_3^{2-}$ ($mmol•L^{-1}$)	5.0	3.3	2.0	4.2	30.7	71.9	24.2	75.2
Hardness ($mmol•L^{-1}$)	112.8	109.9	112.9	113.8	83.2	37.2	56.0	16.8
Turbidity (NTU)	0.5	11.8	16.3	1.1	0.2	1.7	1.1	15.7

Because Ti_3C_2 as the light-to-heat conversion materials was coated on sponge substrate, the concentration of Ti_3C_2 played an important role in solar-driven desalination. To evaluate the effect of the loading concentration of Ti_3C_2 on the evaporation performance, the energy conversion efficiency was investigated by measuring the water evaporation rate of SnO_2-SPM with different Ti_3C_2 loading concentration (0.5, 1.0, 1.5, 2.0 and 2.5 mg•mL^{-1}, denoted by SnO_2-SPM$^{0.5}$, SnO_2-SPM$^{1.0}$, SnO_2-SPM$^{1.5}$, SnO_2-SPM$^{2.0}$ and SnO_2-SPM$^{2.5}$, respectively.). After the light was turned on, the water mass changed because of the vapor production was recorded by a balance. The typical curves of time-dependent mass change were provided in Fig. S20. The SnO_2-SPM$^{2.0}$ exhibited a water evaporation rate of 1.41 kg•m^{-2}•h^{-1} under 1-sun irradiation. By contrast, the water evaporation rate of SnO_2-SPM$^{0.5}$, SnO_2-SPM$^{1.0}$, SnO_2-SPM$^{1.5}$ and SnO_2-SPM$^{2.5}$ was 1.15, 1.28, 1.35, and 1.41 kg•m^{-2}•h^{-1}, respectively (Fig. S21). The solar energy conversion efficiency of absorbers was another important parameter to evaluate the performance of steam generation. As shown in Fig. S21, the water evaporation rate and thermal efficiency gradually increased with the Ti_3C_2 concentration increasing. However, when the concentration of Ti_3C_2 was up to 2.0 mg•mL^{-1}, the evaporation rate and thermal efficiency were almost unchanged even if the Ti_3C_2 concentration was further increased. Hence, 2.0 mg•mL^{-1} of Ti_3C_2 was selected for the following experiments unless otherwise specified.

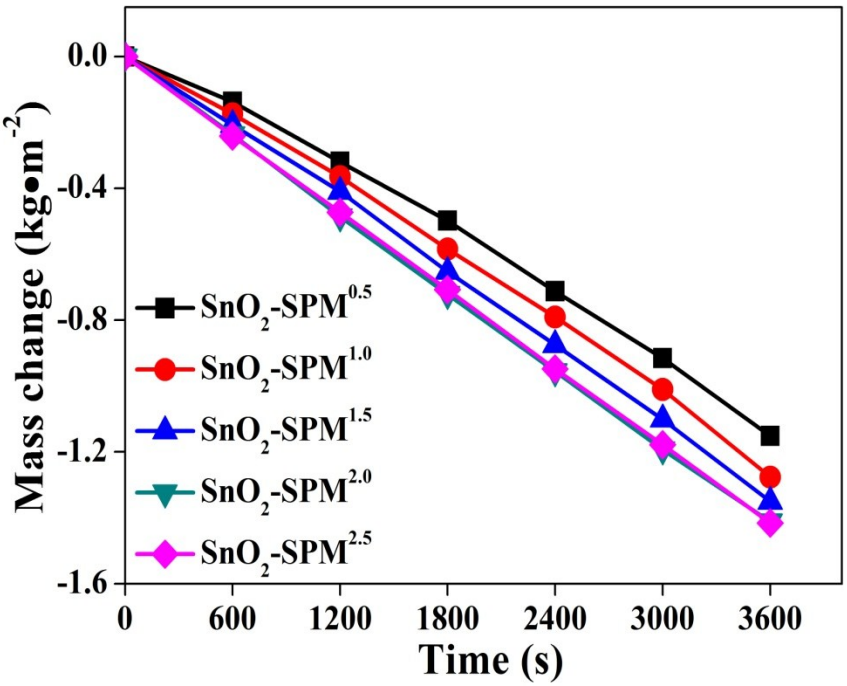

Fig. S20 Mass change of seawater over time by using SnO_2-SPM$^{0.5}$, SnO_2-SPM$^{1.0}$, SnO_2-SPM$^{1.5}$, SnO_2-SPM$^{2.0}$ and SnO_2-SPM$^{2.5}$ under 1-sun irradiation.

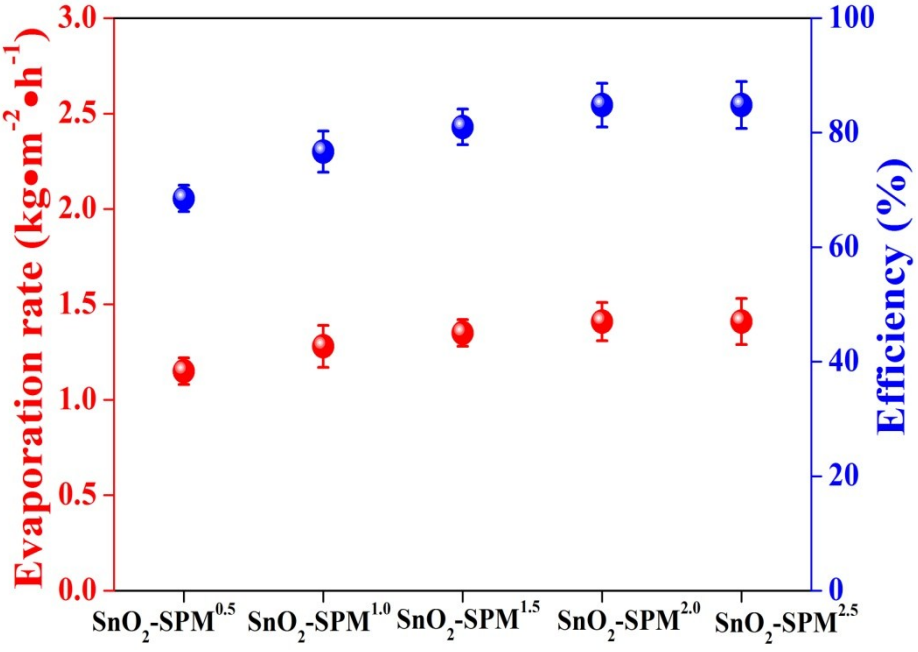

Fig. S21 Thermal efficiency and corresponding evaporation rate for SnO_2-SPM$^{0.5}$, SnO_2-SPM$^{1.0}$, SnO_2-SPM$^{1.5}$, SnO_2-SPM$^{2.0}$ and SnO_2-SPM$^{2.5}$ under 1-sun irradiation.

References

1. R. Y. Li, L. B. Zhang, L. Shi, P. Wang, *ACS Nano*, 2017, **11**, 3752–3759.